Chapter 2
Synchronous Reluctance and PM Assisted Reluctance Motors

Nicola Bianchi

Abstract This chapter focuses on the key notions about analysis and design of synchronous reluctance and permanent magnet assisted synchronous reluctance motors. The aim is to highlight not only the advantages of such machines but also some drawbacks of theirs, such as the low power factor and the torque ripple. The strategies to reduce such drawbacks are also reported. Machines adopting Ferrite magnets instead of rare–earth permanent magnets are considered. The anisotropic structure yields a significant reluctance torque component, compensating the use of low energy PMs. Basic concepts of the motor control and sensorless control are summarised. Some tricks to overcome the torque ripple are described, also when fractional–slot windings are adopted.

Keywords Design of synchronous reluctance machines · Segregation of reluctance and PM torque · Torque ripple · PM assistance · Fractional-slot windings · Sensorless control

2.1 Introduction

The synchronous reluctance (REL) machine with transversally laminated rotor has been proposed several years ago, but only in the last years it is becoming more and more attractive This is due to its robustness, high overload capability, and its low cost. The REL motor is becoming a good competitor in applications requiring high dynamic, high torque density, and fault-tolerant capability. Figure 2.1a shows two four–pole REL motors characterized by two and three flux–barriers per pole, respectively. A permanent magnet (PM) can be inset in each rotor flux–barrier, as in Fig. 2.1b, which shows two motors characterized by two and three flux–barriers per

N. Bianchi (✉)
Department of Industrial Engineering, University of Padova, via Gradenigo 6/A,
35131 Padova, Italy
e-mail: nicola.bianchi@unipd.it

© The Author(s) 2016

G. Pellegrino et al., *The Rediscovery of Synchronous Reluctance and Ferrite Permanent Magnet Motors*, SpringerBriefs in Electrical and Computer Engineering, DOI 10.1007/978-3-319-32202-5_2

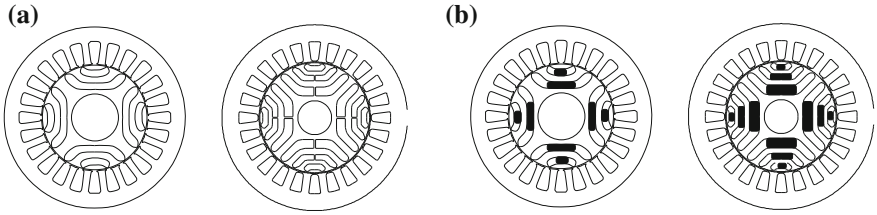

Fig. 2.1 Sketch of four–pole synchronous reluctance motors (**a**) and PM assisted reluctance motors (**b**), with two and three flux–barriers per pole. **a** REL motors. **b** PMAREL motors

pole, respectively. The resulting configuration is called PM assisted synchronous reluctance (PMAREL) machine. Sometimes it is also referred to as Interior PM (IPM) machine, generally when the PM flux tends to be the dominant component of the machine flux [1, 2]. The aim of adopting PMs is manifold: to saturate the rotor iron bridges, to increase the motor torque, to increase the power factor, as it will be pointed out hereafter.

2.2 The Synchronous Reluctance Motor

Let us refer to the four–pole REL machine drawn in Fig. 2.2a There are two different rotor paths for the flux. One is a high permeability path, see Fig. 2.2b, the flux lines flowing in rotor iron paths, parallel to the flux-barriers. It is commonly referred to as the *d*-axis path. The second is a low permeability path, see Fig. 2.2c, since the flux lines have to cross the rotor flux barriers. It is commonly referred to as the *q*-axis path. The final *dq* reference frame is shown in Fig. 2.2d.

The rotor is designed with several flux barriers, in order to obstacle the flux along the *q*-axis and to achieve a high saliency ratio, that is, a high reluctance torque component. This has been presented in Chap. 1. However, iron bridges remain (at the ends and sometimes in the middle of each barrier) to mechanically sustain the rotor parts. A portion of *q*-axis flux flows through these bridges, with a consequent reduction of the torque.

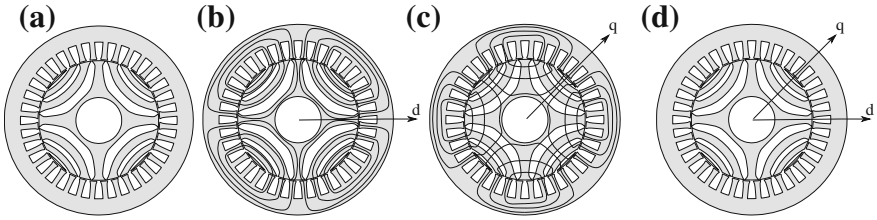

Fig. 2.2 Sketch of a synchronous reluctance motor with **a** geometry, **b** *d*-axis flux lines, **c** *q*-axis flux lines, and **d** reference frame. **a** Configuration. **b** *d*-axis flux. **c** *q*-axis flux. **d** *d*-axis flux

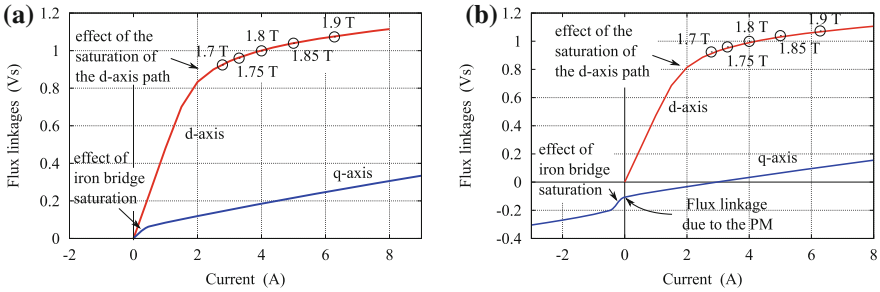

Fig. 2.3 Flux linkages versus currents characteristics. The highest values of flux density are also reported. **a** REL machine. **b** PMAREL machine

Figure 2.3a shows the flux linkage λ_d versus current i_d (with $i_q = 0$), and the flux linkage λ_q versus current i_q (with $i_d = 0$), for a REL machine. For given current, the d-axis flux linkage is is clearly higher. The iron saturation (at higher currents) limits the d-axis flux. Maximum flux density in the stator paths is reported. Let's remember that the inductances are not more constant but they vary with the stator current. Apparent and incremental inductances are different. Discussion about apparent and incremental inductances is given in Chap. 4.

On the contrary, the q-axis flux linkage is lower, since it is limited by the rotor flux barriers. It remains almost linear with the current. At current close to zero, a change of the curve drop is evident. It is due to the saturation of the iron bridges.

Similarly, Fig. 2.3b shows the d- and q-axis flux linkages versus currents of the reference PMAREL motor. When a PM is introduced in the rotor flux–barriers, according to the reference frame defined above, it produces a negative flux linkage along the q-axis. Then, the q-axis flux linkage versus the q-axis current is modified as reported in Fig. 2.3b.

In general, the flux linkages can be expressed as a function of the currents as

$$\begin{aligned} \lambda_d &= L_d i_d \\ \lambda_q &= L_q i_q - \Lambda_m \end{aligned} \tag{2.1}$$

where Λ_m is the flux linkage due to the PM, L_d and L_q are the apparent d- and q-axis inductances, respectively. The inductance L_d (which is related to the main flux of the machine) corresponds to the magnetizing inductance. The inductance Lq is quite low, since it corresponds to the flux obstructed by the flux barriers. Consideration about the optimal design of the motor are reported in Chaps. 3 and 5.

The magnetic model described by (2.1) is a simplified model. At first, when saturation occurs, the inductances have to be considered varying with the currents. In addition, the model does not consider the cross-coupling interaction between the d- and the q-axis. Such a phenomenon will be dealt with in Chap. 4.

The ratio between d-axis and q-axis inductance defines the rotor saliency ξ, that is, $\xi = L_d/L_q$.

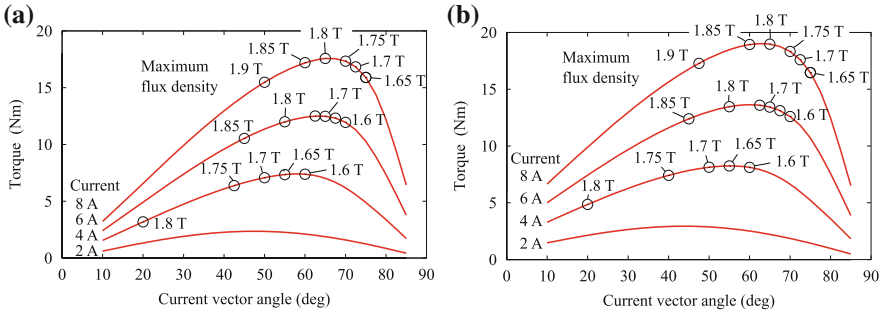

Fig. 2.4 Torque versus current vector angle, varying the stator current amplitude. **a** REL machine. **b** PMAREL machine

Figure 2.4a shows the torque exhibited by the REL motor versus the current vector angle α_i^e, varying the amplitude of the stator current. Again, some values of flux density in the stator tooth are also reported. The higher flux density is achieved when the stator current vector is along the d-axis (i.e., $\alpha_i^e = 0°$), and it decreases when the current vector moves towards the q-axis. The figure highlights the maximum torque that can be reached for a given current (electrical limit). In a similar way, Fig. 2.4b shows the torque exhibited by the PMAREL motor versus the current vector angle α_i^e, varying the stator current amplitude. The highest flux density values in the stator iron are reported so as to highlight the magnetic limits. Using Ferrite magnet, a higher torque is obtained for the same current and flux density limits. A further discussion about the impact of the electrical and magnetic limits on the electromagnetic torque is given in Chap. 3. Figure 2.5a, b show the flux lines and the flux density map at rated current of a REL motor and a PMAREL motor, respectively.

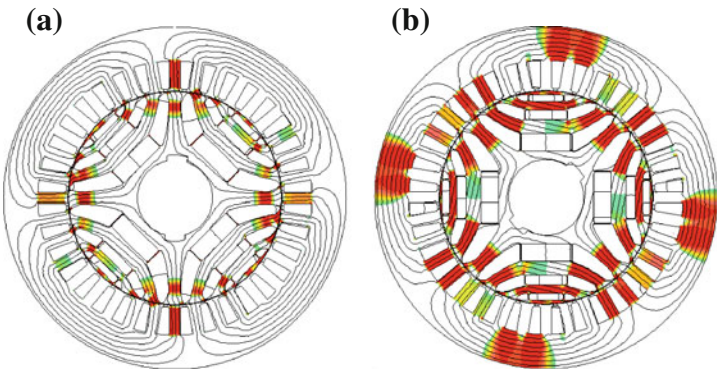

Fig. 2.5 Flux lines and flux density map of REL and PMAREL motor. **a** REL motor. **b** PMAREL motor

2.2.1 Computation of the Torque

With the assumption of a lossless, non-hysteretic magnetic model, the expression of the electromagnetic torque [3, 4] is

$$\tau_{em} = \frac{3}{2}p\left(\lambda_d i_q - \lambda_q i_d\right) - \frac{\partial W_{mc}(i_d, i_q, \vartheta_m)}{\partial \vartheta_m} \tag{2.2}$$

where p is the number of pole pairs. W_{mc} is the magnetic co-energy, expressed as a function of the rotor position ϑ_m and the stator currents i_d and i_q. The average value of the variation of the magnetic co-energy during a rotor turn is zero, therefore this term is generally omitted when referring to the average torque. Thus, only the first term of (2.2) is considered, i.e., $\tau_{dq} = \frac{3}{2}p(\lambda_d i_q - \lambda_q i_d)$. Equation (2.2) has to be used, when the actual behavior of the torque with the rotor position is investigated, including average torque and ripple.

As an example, Fig. 2.6a shows the torque behavior under load of a REL machine, using finite element (FE) analysis. The machine is fed by both d- and q-axis currents. The actual torque is indeed represented by the solid line, that is, the torque computed by means of Maxwell stress tensor. Such a computation highlights an evident torque ripple. On the contrary, the behavior of τ_{dq} (dashed line) is smooth and close to the average torque. Adding the derivative of the magnetic co-energy with the rotor position to the τ_{dq} term, as in (2.2), the resulting torque behavior corresponds exactly to the torque computed using Maxwell stress tensor (the circles result to be almost superimposed to the solid line).

Figure 2.6b shows the torque versus rotor position behavior under load of a PMAREL machine. As for the REL motor, the behavior of τ_{dq} is smooth and close to the average torque. Adding the derivative of the magnetic co-energy with the rotor position, the resulting torque (2.2) corresponds to the Maxwell torque.

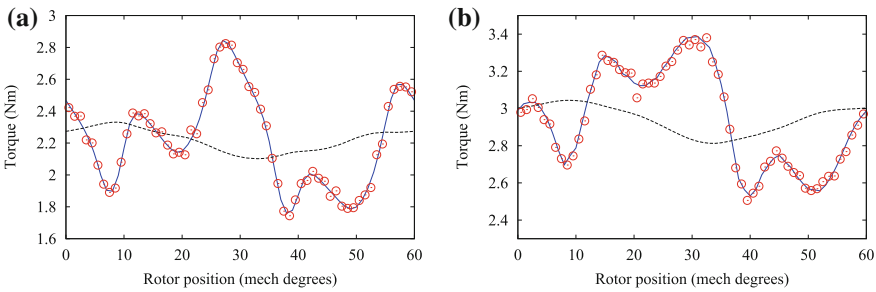

Fig. 2.6 Torque behavior under load according to constant i_d and i_q currents. Solid line refers to the computation using Maxwell stress tensor (from finite element analysis), dashed line refers to the τ_{dq} term, circles refer to the sum of τ_{dq} and the variation of the magnetic coenergy, as in (2.2). **a** REL machine. **b** PMAREL machine

Neglecting the iron saturation and the torque oscillations, the average torque can be espressed as

$$\tau_{em} = \frac{3}{2}p\left(L_d - L_q\right)i_d i_q + \frac{3}{2}p\Lambda_m i_d \tag{2.3}$$

where the first term represents the reluctance torque component and the second term represents the PM torque component, as also defined in Chap. 1. Roughly speaking, it appears that in a REL motor, the torque is due to the difference between the d- and the q-axis inductance. The PM yields a further torque term.

Finally, a magnetic model of the REL machine can be adopted where the electromagnetic quantities in the air gap are highlighted. The reluctance torque is expressed as a function of the stator linear current distribution $K_s(\vartheta_r)$ and the scalar magnetic potential of the rotor $U_r(\vartheta_r)$, the latter due to the magnetic flux crossing the flux barriers. Both of them depend on the angular variable ϑ_r. Such an electromagnetic torque results in

$$\tau_{em} = \frac{\mu_0}{g}\frac{D_s^2 L_{stk}}{4}\int_0^{2\pi} -U_r(\vartheta_r)K_s(\vartheta_r)d\vartheta_r \tag{2.4}$$

where D_s and L_{stk} are the stator inner diameter and the stack length, respectively.

2.2.2 Segregation of the REL and PM Torque Components

It is interesting to split the total electromagnetic torque in its two components: the reluctance torque component and the PM torque component. This is not immediate when the iron saturation occurs, and some preliminary considerations are necessary about the d- and q-axis current and flux linkage.

Due to the symmetry of the magnetic circuit along the d-axis, a positive and negative d-axis current yield a d-axis flux linkage with the same amplitude but opposite sign (the same sign of the current). The torque also reverses its sign when the d-axis current changes from positive to negative.

On the contrary, the q-axis current produces a flux that is in the same direction with the PM flux when the q-axis current is negative, and in the opposite direction when it is positive. Therefore, a different flux linkage is expected depending on the q-axis current sign. When the q-axis current changes its sign, only the reluctance torque component is reversed, while the PM torque component remains almost the same.

For a given couple of currents (I_d, I_q) it is possible to split the electromagnetic torque into its two components: a permanent magnet τ_{pm} and a reluctance τ_{rel} torque component. They are given by:

$$\tau_{pm} = \frac{1}{2}[\tau_{em}(I_d, I_q) + \tau_{em}(I_d, -I_q)] \tag{2.5}$$

$$\tau_{rel} = \frac{1}{2}[\tau_{em}(I_d, I_q) - \tau_{em}(I_d, -I_q)]. \tag{2.6}$$

2.2.3 Vector Diagram of the REL Motor

Figure 2.7 shows the vector diagram of a REL motor. Even though if the d- and q-axis current components are almost equal, the d-axis flux linkage results to be higher than the q-axis flux linkage. The motor is commonly current controlled. The current is supplied so as to achieve the maximum torque per given current. The maximum torque-per-ampere (MTPA) trajectory is achieved with a current vector angle in the first quadrant (if saturation is neglected it results in $\alpha_i^e = 45°$). An example is reported in Fig. 2.8.

2.2.4 Power Factor of the REL Machine

A drawback of the REL motor is the quite low power factor. From the vector diagram of Fig. 2.7: it is worth noticing that the voltage vector leads the current vector and the power factor angle φ is quite high.

The power factor is a function of the rotor saliency ξ. Figure 2.9 shows the power factor versus the motor saliency neglecting iron saturation. The lower curve reports the power factor when the current vector is operated along the MTPA trajectory, that is, $i_d = i_q$ (or $\alpha_i^e = 45°$). It is evident that the power factor is quite low: referring to a saliency $\xi = 10$ it is $\cos\varphi = 0.63$. The second curve refers to

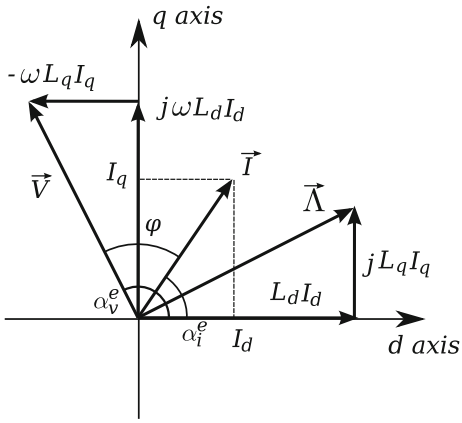

Fig. 2.7 Vector diagram of the REL motor. Current vector is split in its I_d and I_q components. They yield the flux linkages $L_d I_d$ and $L_q I_q$, respectively. The total flux linkage is achieved as vector sum. The voltage vector results by multiplying vector Λ by $j\omega$

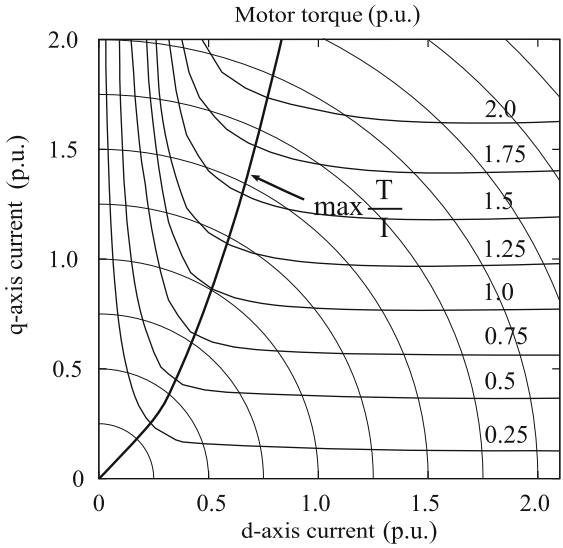

Fig. 2.8 Torque map in the i_d–i_q plane, together with the MTPA trajectory

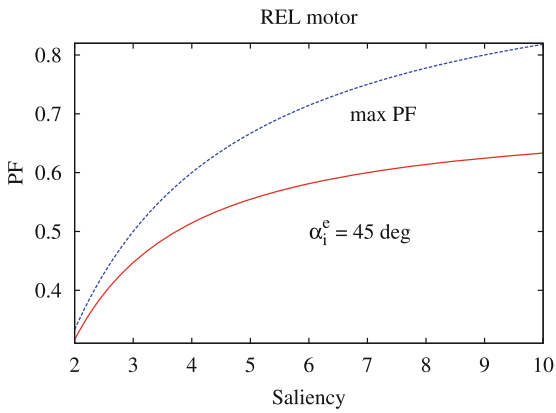

Fig. 2.9 Power factor (PF) as a function of the rotor saliency ξ. Analysis neglecting the iron saturation

operating conditions so as to maximize the power factor. This corresponds to $tan(\alpha_i^e) = \sqrt{\xi}$. A power factor slightly higher than 0.8 is achieved, referring again to $\xi = 10$.

When the iron saturation occurs, the operating current vector is achieved at higher angle α_i^e. Therefore, the power factor tends to increases. This will be discussed in Chap. 3. Anyhow, the volt-ampere ratings of the inverter of a REL motor is commonly 20 %–30 % higher than the motor output power.

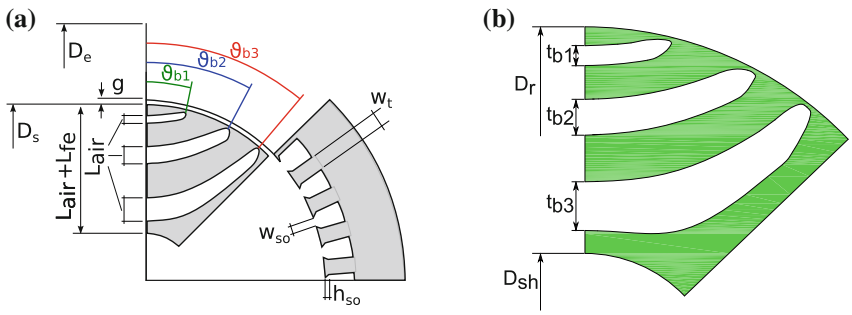

Fig. 2.10 REL motor geometry and variable parameters

2.3 Saturation Effects

The investigation of the impact of the iron saturation on the machine performance is carried out varying the thickness of the flux-barriers. Referring to Fig. 2.10 the coefficient k_{air} is defined as:

$$k_{air} = \frac{L_{air}}{L_{air} + L_{fe}} = \frac{\sum_i t_{bi}}{(D_r - D_{sh})/2} \tag{2.7}$$

where, the terms t_{bi} are the thicknesses of the flux–barriers, D_r is the external rotor diameter and D_{sh} is the shaft diameter. Coefficient k_{air} has to be chosen according to the stator geometry (e.g., tooth width and back–iron height). In this way it is possible to define a coefficient $k_{air,s}$ related to the stator geometry as follow:

$$k_{air,\,s} = \frac{p_s - w_t}{p_s} \tag{2.8}$$

in which p_s is the stator slot pitch defined as: $p_s = \pi D_s / Q_s$ and w_t is the stator tooth width. It is evident that the rotor k_{air} should be close to the stator $k_{air,s}$, so as to get the machine equally saturated.

Simulations have been performed using two different four-pole rotors with three flux-barriers per pole. To determine the convenience of having $k_{air} > k_{air,s}$ or $k_{air} < k_{air,s}$, two extreme cases are considered. Since the stator $k_{air,s} = 0.46$, the rotor coefficients have been selected to be $k_{air} = 0.35$ and $k_{air} = 0.65$ respectively, resulting the geometries in Fig. 2.11.

As will be described in Sect. 2.8, the rotors are designed with different angles of the flux-barrier ends [23, 32], that is, the North pole flux–barriers are slightly different from those in the South pole, so as to minimize the torque ripple. The optimization can be achieved on the basis of an analytical model or adopting a FE model of the motor, as described in Chap. 5.

The results carried out by means of FE analysis highlight differences in term of torque ripple, average torque and power, flux linkages, losses and power factor (PF).

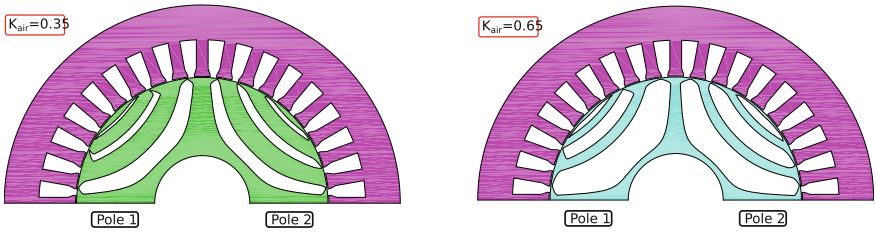

Fig. 2.11 Machine layouts for $k_{air} = 0.35$ and $k_{air} = 0.65$ configurations

Increasing the saturation level (i.e., increasing k_{air}) the flux density in the rotor increases. On the other hand, in the stator the flux density decreases. The flux linkage versus current curves are shown in Fig. 2.12a, pointing out that the main impact of k_{air} is the decrease of d-axis flux linkage due to iron saturation. With higher k_{air} (that is, with larger flux–barrier thicknesses), the d-axis flux linkage decreases at higher current due to iron saturation, about three times the decrease of q-axis flux linkage.

2.3.1 *Torque Ripple, Mean Torque and Power and Power Factor*

As said above, the first part of (2.2) can be adopted to compute the torque vs. speed behaviors and the torque maps. The second term is used to estimate the torque ripple of the machine. Alternatively, the Maxwell stress tensor can be used to this aim. As (2.2) shows, the torque strictly depends on the difference between the d- and q-axis flux linkages, whose variation with k_{air} is reported in Fig. 2.12a.

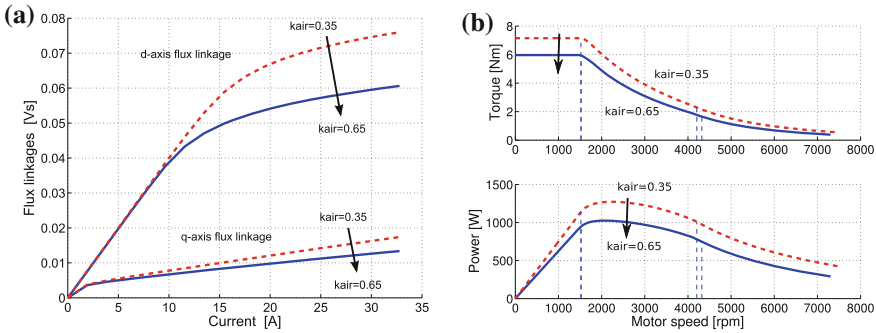

Fig. 2.12 Impact of saturation factor (for $k_{air} = 0.35$ and $k_{air} = 0.65$ configurations): d-axis and q-axis flux linkages (**a**) and torque and power versus speed, when the current vector moves along the optimal MTPA, FW and MTPV trajectories. **a** d-axis and q-axis flux linkages. **b** Torque and power versus speed

Figure 2.12b shows the motor torque and power versus speed for the two REL motors. The optimal current vector trajectory is achieved by means of the Maximum Torque–Per–Ampere (MTPA), FW and Maximum Torque–Per–Voltage (MTPV) points, see Sect. 2.6. The torque and the power decrease as the k_{air} increases. Due to the saturation the MTPA trajectory changes if the k_{air} increases from 0.35 to 0.65. The optimal current phase angle α_i^e in the nominal conditions is equal to 54° with $k_{air} = 0.35$ and equal to 57° with $k_{air} = 0.65$.

2.4 The PM Assistance

As outlined above, there are several advantages when the PMs are inset within the rotor flux–barriers. Figure 2.13 shows a step of the rotor assembling: the PM is going to be inserted in the rotor flux–barrier.

A part of the PM flux tends to saturate the iron bridge in the rotor, as shown in Fig. 2.14. Such a saturation implies a beneficial reduction of L_q [5]. Moreover, the PM added along the negative q-axis compensates the negative flux $L_q I_q$. Referring to the vector diagram shown in Fig. 2.16, the effect of the PM flux linkage is to rotate the flux linkage vector out of phase with respect to the current vector. Since the voltage vector is rotated towards the current vector, the power factor increases.

Fig. 2.13 Insertion of the assisting PMs in the REL rotor flux–barriers

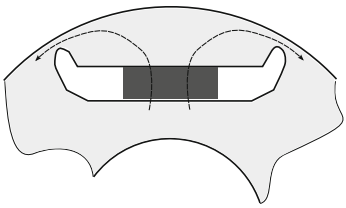

Fig. 2.14 Part of the PM flux flows into the iron bridges

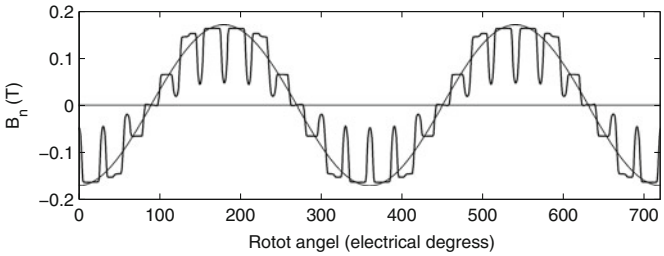

Fig. 2.15 Air–gap flux density distribution. The fundamental harmonic is also reported. The flux density is quite low in a PMAREL machine

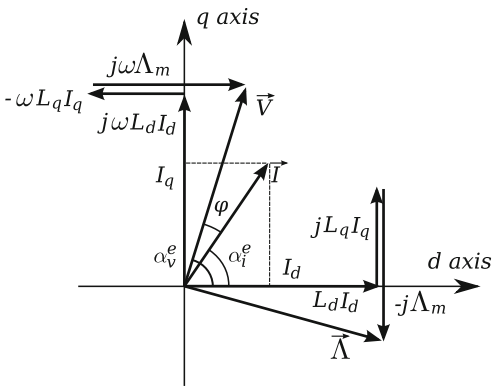

Fig. 2.16 Vector diagram of PMAREL motor

Therefore, the PMAREL motor requires lower Volt–Ampere rating for given nominal mechanical power. Finally, the electromagnetic torque of the motor increases, because a PM torque term is added to the reluctance torque term, as observed in (2.3).

Figure 2.15 shows the air–gap flux density distribution, together with the fundamental waveform, due to the PM magnet in the rotor. In order to maintain the intrinsic fault-tolerant capability of the REL machine, the added PM is minimum. Then, the back EMF is low, the short–circuit current is low [6] as well as the corresponding braking torque [7]. The PM flux is quite low, especially when Ferrite magnets are adopted.

2.4.1 Performance Comparison Between REL and PMAREL Motor

Figure 2.17a compares the torque and power behaviours of a REL and a Ferrite PMAREL motors. These behaviors have been obtained following the MTPA

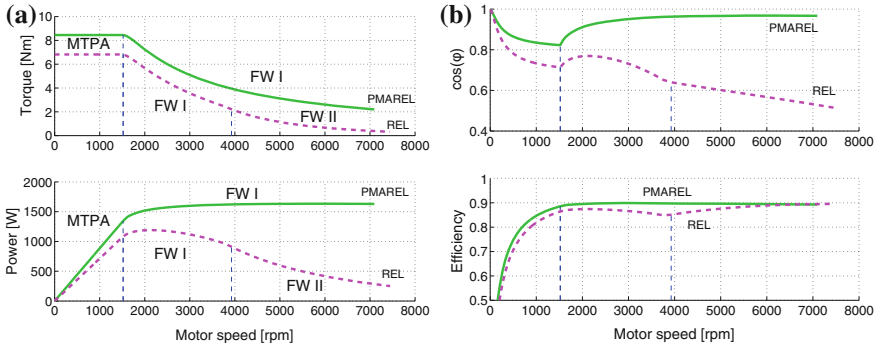

Fig. 2.17 Torque, power, power factor and efficiency for PMAREL and REL configurations, when the current vector moves along the optimal MTPA, FW and MTPV trajectories. In the PMAREL machine, I_{ch} is about $0.75I_n$. **a** Torque and power. **b** Power factor and efficiency

trajectory, FW region I (constant current, constant voltage) as well as FW region II (decreasing current, constant voltage), also called MTPV trajectory. Vertical dashed lines separate operating FW regions I and II [8, 9]. It is worth noticing that the PMAREL configuration does not reach the FW region II in the considered speed range.

Adding the PM, the base torque increase is about 25 %. The power in FW operations increases up to 1500 W and remains constant up to the maximum speed. Such a behavior is due to the fact that the PM has been chosen so as to achieve the characteristic current I_{ch} close to the nominal current I_n. The short-circuit current at steady-state (also called characteristic current) is defined as $I_{ch} = \Lambda_m/L_q$ [10]. The optimal flux-weakening design line is reported in Chap. 1.

Figure 2.17b shows another important effect of adding PMs, that is, the increase of the power factor in the whole operating region. The power factor is always above 0.8 and always higher than the REL machine. The power factor improvement due to the PMs is more beneficial as the speed increases. It means that the size of the converter could be lower for the same base torque adopting the PMAREL solution. Finally, as shown in the bottom of Fig. 2.17b, the efficiency of the PMAREL motor results to be also higher of that of the REL machine.

2.4.2 Optimal PM Flux Linkage

An optimal PM flux linkage can be found so as to maximize the torque of the PMAREL motor, according to given (i.e., nominal) current and flux linkage. The allowable current is limited by the motor and/or inverter rating and represents a maximum electric loading limit. The allowable flux linkage is limited at low speeds by the magnetic loading in the machine. Together with the current limitation, this defines the maximum low–speed torque output. The low-speed torque is

proportional to the product of the flux linkage magnitude, the current magnitude and the sine of the angle between the phasors. This is equivalent to the torque being proportional to the magnetic loading, electric loading and the sine of the angle between them.

The optimal flux linkage results in

$$\Lambda_m = \frac{\Lambda_n}{\sqrt{\left(\frac{L_d I_n}{\Lambda_n}\right)^2 + 1}} \left[\frac{1}{\xi}\left(\frac{L_d I_n}{\Lambda_n}\right)^2 + 1\right] \tag{2.9}$$

The corresponding currents are given by

$$I_d = I_n \frac{1}{\sqrt{\left(\frac{L_d I_n}{\Lambda_n}\right)^2 + 1}} \text{ and } I_q = I_n \frac{\frac{L_d I_n}{\Lambda_n}}{\sqrt{\left(\frac{L_d I_n}{\Lambda_n}\right)^2 + 1}} \tag{2.10}$$

It is worth noticing that the $d - q$ currents in (2.10) follow the trajectory to get the maximum power factor. In addition, the PM flux linkage required from (2.9) is quite high. Figure 2.18 shows the optimal PM flux linkage (in p.u.) as a function of the rotor saliency ξ, for three values of d-axis inductance. It is worth noticing that the required PM flux linkage is quite high, even with high saliency ratio and high d-axis inductance.

The maximum power factor current control is not always adopted. The more common control is to select the current vector so as to achieve the Maximum Torque per Ampere (MTPA) ratio, even if this involves a higher Volt-Amps power rating. Hereafter, the constraint to work along the MTPA trajectory has to be

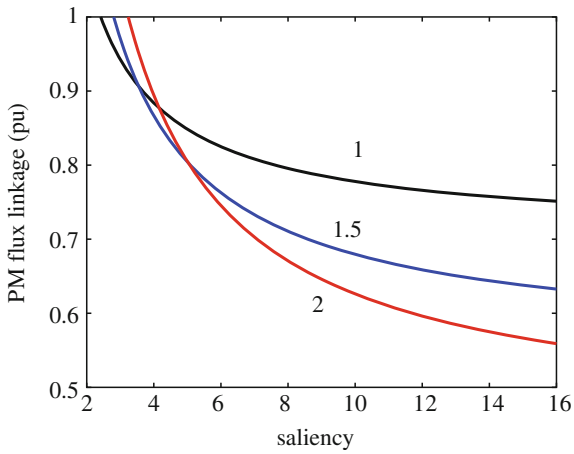

Fig. 2.18 Optimal PM flux linkage versus the motor saliency $\xi = L_d/L_q$ (L_d = 1.0, 1.5, and 2.0 p.u.)

imposed in the analysis. Of course, such a position corresponds to add a further constraint to the d- and q-axis currents. The current vector angle α_i^e has to satisfy the relationship

$$\sin \alpha_i^e = \frac{\sqrt{\Lambda_m^2 + 8(L_d - L_q)^2 I_n^2)} - \Lambda_m}{4(L_d - L_q)I_n} \tag{2.11}$$

Therefore, the nominal flux linkage Λ_n is fixed (e.g., 1 p.u.), the saliency ratio ξ and the PM flux linkage Λ_m are kept as variables, and the inductances (the d-axis inductance L_d and the q-axis inductance $L_q = L_d/\xi$) are adjusted to satisfy the constraint of unity nominal flux linkage.

The impact of the choices to select the PM flux linkage on the performance of the machine is shown in Table 2.1. A saliency ratio $\xi = 10$ is fixed. Specific choices of PM flux linkage have been fixed (the first column of the table). Note that $\Lambda_m = L_q I_q$ means a PM flux linkage that balances the q-axis flux due to the current; and $\Lambda_m = L_q I_n$ means a PM flux linkage that forces the nominal current in the event of short circuit. Then, current angle α_i^e is computed from (2.11), the inductances are adjusted and the motor performance is computed. Since the iron saturation is neglected, an evident overestimation of the motor fluxes and torque is expected, therefore the results have to be considered as comparison terms, and not as absolute values.

The resulting PM flux linkage is quite lower than that achieved from the previous optimization (Fig. 2.18). This is reasonable using Ferrite magnets. However, it is worth noticing that a power factor higher than 0.8 is achieved only if the PM flux linkage Λ_m is at least three times the $L_q I_n$.

Table 2.2 shows some results achieved by means of finite element (FE) analysis, neglecting iron saturation (the iron bridges in the rotor are substituted by small open slots). The saliency ratio results about 15. Reference motor is the REL motor, whose results are reported in the first row. Then, a PM is included in the rotor in order to assist the REL motor. PM property and PM width h_m are varied so as to modify the PM assistance: this is quantified by means of the equivalent airgap flux density due to PM, which is expressed as the ratio between the remanent flux of the PM and the air gap surface corresponding to one pole. It is:

Table 2.1 Impact of choice of PM flux linkage (current along the MTPA trajectory). Saliency ratio is $\xi = 10$

Setting	Λ_m (p.u.)	L_d (p.u.)	I_d (p.u.)	I_q (p.u.)	τ_{dq} (p.u.)
$\Lambda_m = L_q I_q$	0.095	1.379	0.725	0.688	0.688
$\Lambda_m = 2L_q I_q$	0.180	1.343	0.742	0.671	0.735
$\Lambda_m = 3L_q I_q$	0.256	1.304	0.756	0.655	0.774
$\Lambda_m = L_q I_n$	0.136	1.362	0.733	0.680	0.711
$\Lambda_m = 2L_q I_n$	0.260	1.301	0.757	0.654	0.776
$\Lambda_m = 3L_q I_n$	0.369	1.230	0.778	0.629	0.828

Table 2.2 Comparison of FE analysis results without including iron saturation (with fixed limit stator current)

$B_{g,eq}$ (T)	Λ_m (Vs)	α_i^e (deg)	Λ_d (Vs)	Λ_q (Vs)	Λ (Vs)	T (Nm)	$\cos\phi$
0	0	45	1.109	0.073	1.111	6.6	0.66
0.100	0.15	45	1.109	−0.076	1.112	7.5	0.75
0.201	0.30	45	1.108	−0.226	1.131	8.5	0.83
0.302	0.45	45	1.109	−0.376	1.171	9.5	0.90
0.403	0.60	48	1.050	−0.522	1.173	10.2	0.96
0.604	0.75	52	0.966	−0.667	1.174	10.6	0.99
0.645	0.96	56	0.877	−0.873	1.237	10.9	0.98
0.665	0.99	61	0.761	−0.898	1.177	9.9	0.93
0.685	1.02	68	0.588	−0.923	1.094	8.0	0.81
0.705	1.05	74	0.433	−0.949	1.043	6.1	0.65

$$B_{g,eq} = \mu_{rec}\mu_0 H_c \frac{2ph_m}{\pi D_i} \tag{2.12}$$

where μ_{rec} is the PM relative differential permeability, H_c is the PM coercive field strength.

Let's note that a small PM flux (corresponding to $B_{g,eq}$ = 0.1 T) is enough to reverse the q-axis flux. Such a PM flux corresponds to using Ferrite magnets only in the middle of the three flux barriers, according to a rotor geometry as shown in Fig. 2.5a. It is also noticing that, with a PM flux linkage in the range between 25 % and 35 % of the nominal (total) flux, the power factor results to be higher than 0.8.

The magnetic limit is reached when the PM flux corresponds to $B_{g,eq}$ = 0.403 T. With higher PM flux, the torque increases again, even if the increase of the torque is more and more slight. The maximum torque is found at $B_{g,eq}$ = 0.645 T. However, such a maximum is quite flat. For a higher PM flux, the magnetic limit is dominant, and the allowed operating point moves far from the optimum point. The torque decreases even if the current amplitude remains the same. The maximum torque is achieved with a large amount of PM flux: a PM flux linkage at least 60 % of the total. In this case the PM "assistance" is very significative, maybe too high to classify this motor as a PMAREL motor. From a practical point of view, it is reasonable not to exceed with the PM flux, even because the maximum of the torque is quite flat.

2.5 Comparison Between Predictions and Measurements

Motor capability is tested by means of the test bench shown in Fig. 2.19. The motor under test is connected to a master motor, and a torquemeter is mounted between the two shafts. The master motor maintains a fixed speed and it operates as a brake.

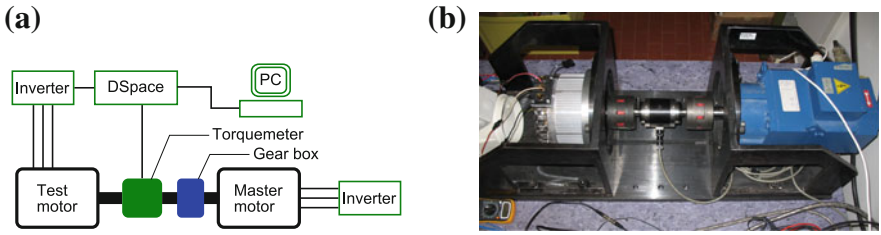

Fig. 2.19 Experimental setup for motor testings. The motor under test is on the left hand side. The master machine is on the right hand side. The torquemeter can be seen between the two machines. **a** Measure scheme. **b** Photo of the test bench (gear-box is not included)

A wattmeter measures the input electric power, P_{in}. The measured torque is instead used to compute the output mechanical power at the shaft, P_{out}.

To determine the average torque and the torque ripple in various operating conditions, low speed tests are carried out, introducing a gear box with a high gear ratio. The gearbox is non–reversible to avoid that torque ripple of the master motor is transmitted on the torquemeter shaft. To obtain a more precise measurement, the torque is measured for several turns of the rotor, and then its average value is achieved, so as to reduce the measurement noise.

From the low-speed tests, it is also possible to determine the Maximum Torque Per Ampere (MTPA) current trajectory. From the high-speed tests, the steady–state motor performance is measured, including efficiency and FW capability.

As an example, Fig. 2.20a shows some measured torque versus rotor position behaviours feeding the motor with different current amplitudes. From these tests, it is possible to achieve the average torque and the torque ripple amplitude.

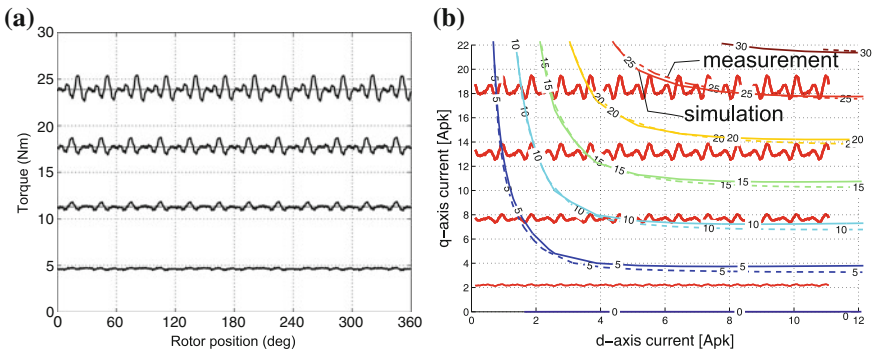

Fig. 2.20 Comparison between experimental results (continuous line) versus FE simulation (dashed line) on the REL motor (without rotor skewing). **a** Torque versus rotor position. **b** Torque map

Figure 2.20b shows a comparison between the measured average torque and the torque that has been predicted from FE analysis. Constant torque curves are reported in the I_d-I_q plane. FE results are in solid line and the measurements in dashed line. There is a good agreement between tests and predictions, in a wide operating condition range, including overload, where high saturation occurs in the iron paths.

Further tests of average torque and ripple are reported in Chaps. 4 and 5.

Tables 2.3 and 2.4 report some measurements at steady-state operations. The speed has been selected quite low, to limit the iron losses, so as to have a better investigation of the motor magnetic behaviour. The comparison is carried out for

Table 2.3 REL motor: steady state operations

n (rpm)	T (Nm)	I (A)	I_d (A)	I_q (A)	PF^* (—)	η (%)
250	2	2.26	2.04	2.48	0.64	52
	4	3.35	2.86	3.84	0.72	58
	6	4.4	3.33	5.31	0.78	58
	8	5.39	3.77	6.73	0.81	57
	10	6.42	4.24	8.12	0.83	54
	12	7.43	4.64	9.59	0.85	52
500	2	2.25	2.04	2.48	0.70	61
	4	3.34	2.86	3.84	0.75	69
	6	4.38	3.33	5.31	0.79	71
	8	5.38	3.77	6.73	0.82	70
	10	6.38	4.24	8.12	0.83	69
	12	7.44	4.64	9.59	0.84	67

PF^* = Power Factor

Table 2.4 PMAREL motor: steady state operations

n (rpm)	T (Nm)	I (A)	I_d (A)	I_q (A)	PF^* (—)	η (%)
250	2	2.00	2.10	1.91	0.71	68
	4	3.07	2.98	3.15	0.78	66
	6	4.06	3.46	4.59	0.84	64
	8	5.03	3.94	5.92	0.87	62
	10	6.03	4.50	7.24	0.88	59
	12	6.99	4.84	8.62	0.90	57
500	2	2.00	2.10	1.91	0.77	79
	4	3.07	2.98	3.15	0.81	77
	6	4.06	3.46	4.59	0.86	77
	8	5.03	3.94	5.92	0.87	75
	10	6.03	4.50	7.24	0.88	73
	12	6.99	4.84	8.62	0.89	71

PF^* = Power Factor

given torque values (from 2 to 12 Nm). The d- and q-axis currents are selected so as to operate along the MTPA trajectory.

Even though the PM is a low–energy (Ferrite) magnet, it is worth noticing that the insertion of the PMs allows a lower stator current to be required. As a consequence, the efficiency η increases. At low speed, the motor efficiency results to be quite low. Anyway, for given torque, the use of PMs yields a loss reduction.

The voltage is far from a sinusoidal waveform, the motor being supplied by a power inverter. The rms voltage measured by the wattmeter does not correspond to the rms value of the fundamental voltage harmonic. To improve the measure, the voltages from the inverter output have been filtered before the connection to the wattmeter. The power factor (PF^*) measured in this way is reported in the two tables, which has to be considered an approximation of the commonly definited motor PF (i.e., based on sinusoidal waveforms). Anyway, it is possible to observe an increase of this index in the PMAREL motor. A higher increase is expected when comparing the fundamental harmonic waveforms.

2.6 Vector Control

The vector control of REL and IPM motor drives is commonly described using the circle diagram: the constant torque curves, the voltage limit and current limit curves are drawn on a plane, whose axes are the d-axis current and the q-axis current [9, 10]. In such a plane, the current limit defines a circle whose center is the origin of the plane. The voltage limit defines a family of ellipses, centered in the point $(0, \Lambda_m/L_q)$, whose major–to–minor axis ratio is equal to the saliency ratio ξ. Finally, the torque equation defines a family of hyperbolas. Figure 2.21 shows the corresponding circle diagram.

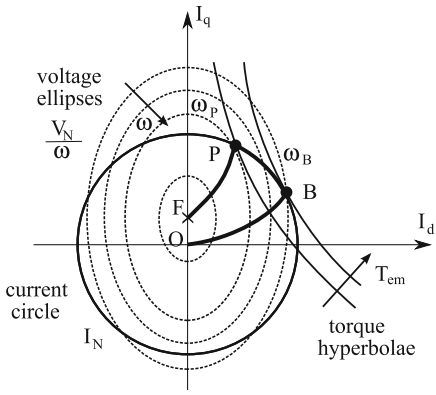

Fig. 2.21 Circle diagram of a PMAREL motor drive

2.6.1 Maximum Torque–Per–Ampere Control

For a given torque demand, the current vector is controlled so as to achieve the minimum current amplitude. The trajectory corresponding to the maximum torque to current ratio is referred to as the maximum torque–per–Ampere (MTPA) trajectory. It is from point O to point P in Fig. 2.21.

Neglecting the iron saturation, the MTPA trajectory of a REL motor is a straight line described by the current vector angle $\alpha_i^e = 45°$. In case of iron saturation (along the d-axis path), α_i^e tends to increase. In case of PMAREL motor, the MTPA trajectory is described by the relationship (2.11) [8].

2.6.2 Flux Weakening Control

In order to operate the motor at a speed higher than the base speed, point B in Fig. 2.21, the flux weakening (FW) control is adopted [12]. The current vector angle α_i^e is increased, so as to decrease the d-axis current, that is, the main flux in the machine. The current amplitude remains the same, so that the current vector moves along the current limit circle I_n, from B to P in Fig. 2.21. When the trajectory of the maximum torque per voltage (MTPV) is reached, point P in Fig. 2.21, at higher speeds the current vector follows such a trajectory, towards the center of the voltage limit ellipses. This happens adopting REL motors (infinite speed is reached at the origin of the axis) and PMAREL motors with $\Lambda_m < L_q I_n$.

When the PM flux linkage is quite high, i.e., $\Lambda_m > L_q I_n$, the center of the ellipses is outside the current limit. Therefore, the operating point P does not exist. The constant volt–ampere region ends at the operating point of the current circle which lies on the I_q-axis, where the torque falls down to zero. This maximum speed is calculated imposing $I_d = 0$ and $I_q = I_n$, yielding

$$\omega_{max} = \frac{V_n}{L_q I_n - \Lambda_m} \tag{2.13}$$

A practical example is reported in Chap. 4. In addition, the block scheme of the control is reported.

2.7 Sensorless Technique by Means of High Frequency Voltage Injection

The sensorless technique by means of high frequency voltage injection on REL and IPM motors takes advantage of the magnetic rotor saliency. High frequency voltage components (of amplitude V_{dh} and frequency ω_h) are usually added on the source

voltages to the aim of detecting the rotor position at low and standstill speed [11, 13, 14].

Considering small flux and current oscillations nearby the operating point, a small–signal linearized model is considered hereafter where $L_{dh} = \partial\lambda_d/\partial i_d$ and $L_{qh} = \partial\lambda_q/\partial i_q$ are the differential d- and q-axis inductances, and $L_{dq} = \partial\lambda_d/\partial i_q = \partial\lambda_q/\partial i_d$ is the cross–saturation inductance. The latter corresponds to the mutual differential inductance between the d- and the q-axis windings.

Therefore, according to the small–signal flux linkages $\delta\lambda_d$ and $\delta\lambda_q$, the small–signal currents result in

$$\delta i_{dh} = \frac{L_{qh}\delta\lambda_{dh} + L_{dq}\delta\lambda_{qh}}{L_{dh}L_{qh} - L_{dq}^2} \text{ and } \delta i_{qh} = \frac{L_{dh}\delta\lambda_{qh} - L_{dq}\delta\lambda_{dh}}{L_{dh}L_{qh} - L_{dq}^2} \tag{2.14}$$

In the following, a rotating high frequency $d-q$ voltage signal is assumed to be injected in the stator winding. Then, the corresponding flux linkages become

$$\delta\lambda_{dh} = \frac{V_h}{\omega_h}\cos(\omega_h t) \text{ and } \delta\lambda_{qh} = \frac{V_h}{\omega_h}\sin(\omega_h t) \tag{2.15}$$

The corresponding high frequency currents are computed from (2.14), resulting in

$$\delta i_{dh} = \frac{V_h}{\omega_h}\frac{L_{qh}\cos(\omega_h t) + L_{dq}\sin(\omega_h t)}{L_{dh}L_{qh} - L_{dq}^2} \text{ and } \delta i_{qh} = \frac{V_h}{\omega_h}\frac{L_{dh}\sin(\omega_h t) - L_{dq}\cos(\omega_h t)}{L_{dh}L_{qh} - L_{dq}^2} \tag{2.16}$$

When the motor is operating in the generic (I_d, I_q) working point, the high frequency current trajectory is an ellipse, as reported in Fig. 2.22. The major and minor axis of such an ellipse, i.e., ΔI_{max} and ΔI_{min}, as well the angle ε between the major axis and the d-axis, are strictly dependent on the values of the differential inductances of the motor, L_{dh}, L_{qh}, and L_{dq} in that particular operating point (I_d, I_q).

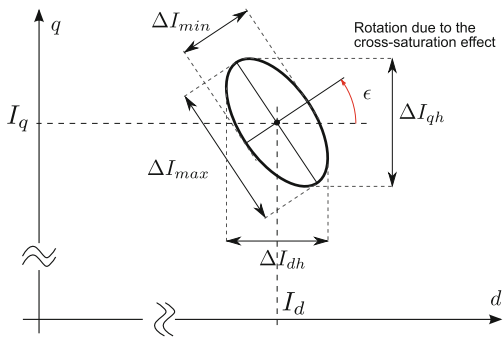

Fig. 2.22 High frequency current trajectory

The detectable high frequency saliency can be defined as the ratio between the current oscillation along the maximum ellipse axis and the minimum ellipse axis, that is

$$\xi_h = \frac{\Delta I_{max}}{\Delta I_{min}} = \frac{L_{avg} + \sqrt{L_{dif}^2 + L_{dq_h}^2}}{L_{avg} - \sqrt{L_{dif}^2 + L_{dq_h}^2}} \tag{2.17}$$

where $L_{avg} = (L_{dh} + L_{qh})/2$ and $L_{dif} = (L_{qh} - L_{dh})/2$. The angular displacement ε of the ellipse depends on the $d - q$ cross-saturation inductance [15], as shown in Fig. 2.22. This angle represents the angular error in the position estimation, and it is computed as

$$\varepsilon = \frac{1}{2}\arctan\left(-\frac{L_{dq}}{L_{dif}}\right) \tag{2.18}$$

2.8 Torque Ripple

The interaction between the spatial harmonics of electrical loading and the rotor anisotropy causes a high torque ripple. This is a common drawback of the REL and PMAREL machines [16].

In [17] it has been shown that the rotor skewing (commonly adopted in PM machines [18, 19]) is not enough to smooth the torque. In any case, only a step–skewing is possible when PMs are used: the rotor is split in two or more parts, each of them is skewed with respect to the others. Figure 2.23 shows the measured torque versus the mechanical position for the REL motor, when it is supplied at rated current, without and with rotor skewing. The torque ripple decreases from about 17 % to about 9 % of the average torque. A similar reduction is found in PMAREL motors.

It has been also shown that a reduction of the torque ripple can be achieved by means of a suitable choice of the number of flux–barriers with respect to the number of stator slots. In this case the flux–barrier ends are uniformly distributed along the

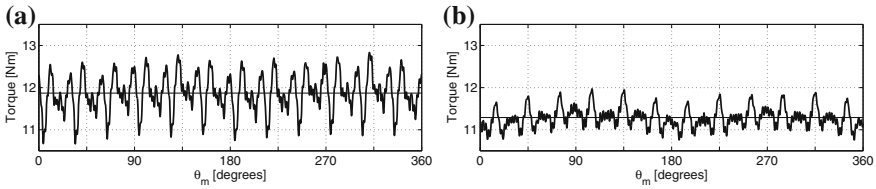

Fig. 2.23 Measured torque versus mechanical position of REL motor with and without rotor skewing. The motors are tested at rated current. **a** Non skewed rotor. **b** Skewed rotor

air–gap (similarly to the stator slot distribution). Optimization of flux-barrier geometry is presented in Chap. 5, together with some experimental tests.

In [20] and then in [21], the flux–barriers are shifted from their symmetrical position. In this way, a sort of compensation of the torque harmonics is achieved. This technique is similar to that proposed in [22] for cogging torque reduction in surface–mounted PM motors.

Alternatively, a strategy to compensate the torque harmonics of the REL motor is presented in [23]. It is based on a two–step design procedure. At first, a set of flux–barrier geometries is identified so as to cancel a torque harmonic of given order. Then, couples of flux–barriers belonging to this set are combined together so as the remaining torque harmonics of one flux–barrier geometry compensate those of the other geometry. This second step can be achieved in two ways:

(i) Stacking the rotor with laminations of two different kinds, the resulting motor is called "Romeo and Juliet" motor, since it is formed by two different and inseparable kinds of lamination. The "Romeo and Juliet" rotor laminations are shown in Fig. 2.24.

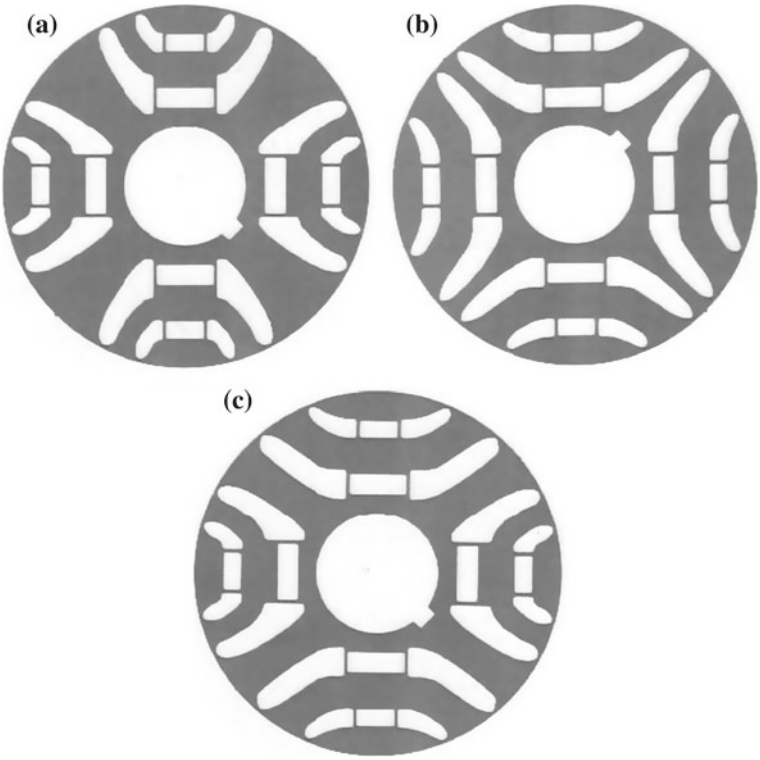

Fig. 2.24 Photos of the "Romeo and Juliet" laminations and of the "Machaon" lamination. In the center of each flux–barrier rectangular holes are designed to address the PMs. **a** **R**–type and **J**–type laminations. **b** "Machaon" lamination

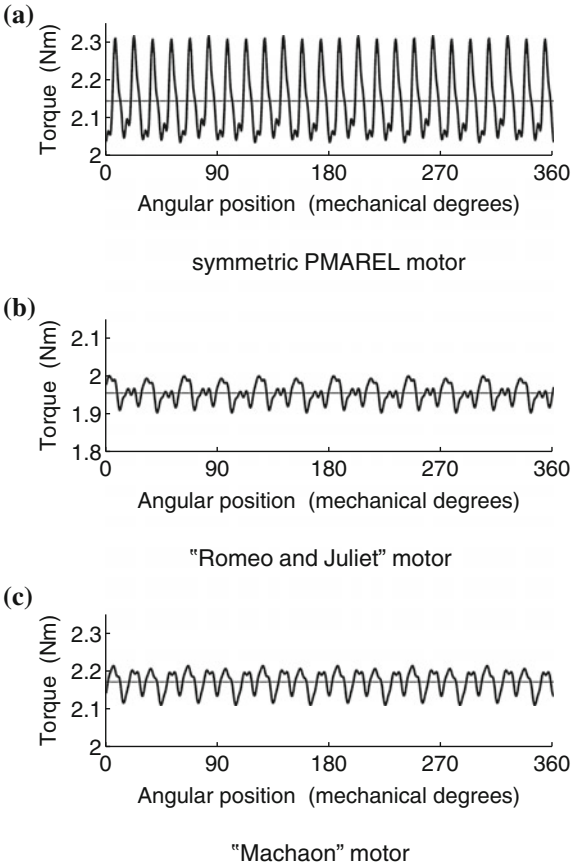

Fig. 2.25 Comparison of the torque behaviours measured on motor prototypes. **a** Symmetric PMAREL motor. **b** "Romeo and Juliet" motor. **c** "Machaon" motor

(ii) Adopting two different flux–barrier geometries in the same lamination, the resulting motor is referred to as "Machaon" motor (the name of a butterfly with two large and two small wings), since the flux–barriers of the adjacent poles are large and small alternatively. The "Machaon" rotor lamination is shown in Fig. 2.24b.

Figure 2.25 shows the measured torque behaviors of a PMAREL motor with symmetrical flux–barrier rotor, a "Romeo and Juliet" rotor and a "Machaon" rotor, referred to the nominal current. The torque ripple of the "Romeo and Juliet" and the "Machaon" motor is about one third of the torque ripple of the PMAREL motor with symmetrical flux–barriers.

Table 2.5 Comparison among SPM and Ferrite PMAREL machines for the same output torque

		PM type:	NdFeB	Ferrite		
Number of slots	Q		27	27	27	24
Number of poles	$2p$		6	6	4	4
Stack length	L_{stk}	(mm)	100	123	113	108
Average torque	T_{avg}	(Nm)	17.3	17.3	17.3	17.3
Total weigth		(kg)	18.3	22.1	20.3	20.5
Total cost		(USD)	67.7	46.4	45.6	48.4

In the economical comparison, material costs are fixed: NdFeB PMs 70 USD/kg, Ferrite PMs 7 USD/kg, copper 8.5 USD/kg, iron lamination 1.1 USD/kg

2.9 Replacing Rare–Earth PMs

Due to the high oscillations of rare–earth material price in the last years, the motor producers are reconsidering the opportunity to use cheaper PMs, such as Ferrite PMs or MQ2 PMs, described in the Chap. 1. A PMAREL machine with Ferrite permanent magnets is compared in [24] to a surface–mounted PM machine with rare-earth PMs. Table 2.5 reports a comparison among weight, and material cost of four machines exhibiting the same torque. The torque density of the Ferrite PM motors is slightly lower, and they have been lengthened to achieve the same performance, even if the increase of the stack length results to be lower than 15 %. From such a comparison the economical convenience of adopting a lengthened Ferrite machine that exploits the reluctance torque mechanisms is evident. The Ferrite PMAREL machines results a good competitor of the surface–mounted PM machine even if the PMs volume has been almost doubled. In addition, the adoption of Ferrite PMs could avoid the uncertainty due to the exceptional price variations of the NdFeB PMs. Further comparisons between machines adopting rare-earth PMs and Ferrite PMs are reported in Chap. 3.

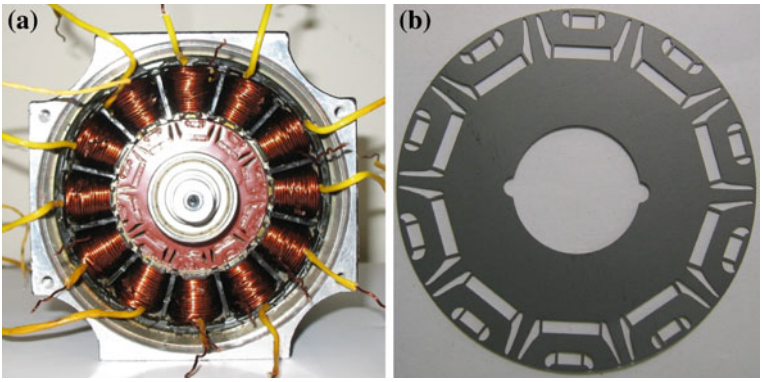

Fig. 2.26 Prototype of a fractional–slot 12–slot 10–pole IPM machine: the stator adopts non-overlapped coils and the rotor is characterized by two flux–barriers per pole

2.10 Fractional-Slot Winding Configurations

Fractional-slot non–overlapped coils are commonly adopted for the stator winding to shorten the end winding length. This yields a considerable reduction of the copper winding and the total cost of the machine [25, 26]. As an example, Fig. 2.26 shows a 12–slot 10–pole motor, whose rotor lamination is characterized by two flux–barriers per pole.

In fractional–slot winding machine, the reluctance torque component is reduced, even though two or three flux-barriers per pole are adopted. The dominant torque component is due to the PM flux. Thus, it is appropriate to refer to that as an IPM machine.

In addition, the fractional–slot configurations allow to increase the fault-tolerant capability of the machine. For instance, fractional–slot windings with non–overlapped coils yield a physical separation between the phases, making the motor to be suitable for fault-tolerant applications [27]. A further solution is the dual–three phase machine, which is sketched in Fig. 2.27 [28]. It is characterized by two identical windings, each supplied by a separate inverter. In the event of a fault of a motor part or one inverter, the corresponding inverter is switched off and only the healthy winding continues to be supplied. Power cutback is equal to half the nominal motor power.

However, when the anisotropic rotor is adopted within a fractional–slot machine, to achieve a smooth torque is a challenge [29–32]. A two–step optimization has been proposed to reduce the torque ripple of REL and IPM motors with fractional–slot winding [33]. At first, the winding is optimized adopting a multi-layer structure so that the harmonic content in the MMF is reduced: it is possible to reduce the winding factor and thus the amplitude of the MMF sub-harmonic. For instance, when the winding is rearranged from a single-layer to a two–layer winding, the

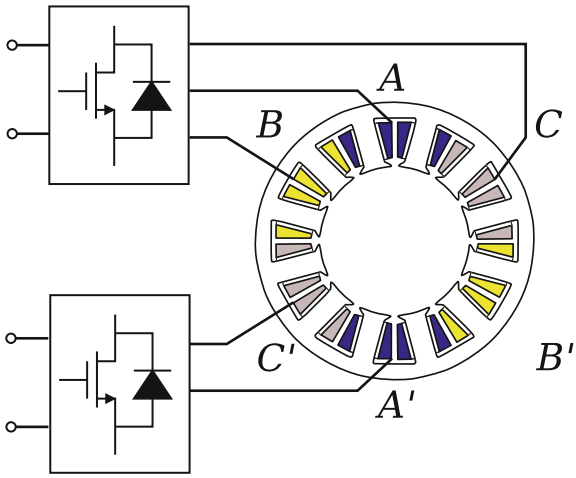

Fig. 2.27 Scheme a dual–three phase fractional–slot IPM machine

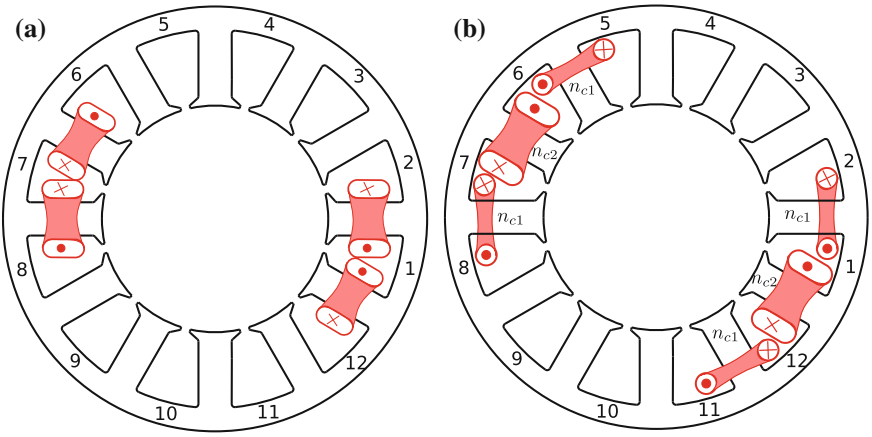

Fig. 2.28 Layouts of the 12–slot 10–pole winding (only coils of one phase are shown). **a** Two-layer winding. **b** Four-layer optimized winding

winding factor of the sub-harmonic reduces to one fourth. The two–layer winding is shown in Fig. 2.28a.

A further reduction of MMF harmonics is achieved when the four–layer winding is adopted, as in Fig. 2.28b. Then, it is also possible to optimize the winding adjusting the number of conductors of the coils, i.e., n_{c1} and n_{c2} in Fig. 2.28b, so that specific harmonics are canceled. It can be demonstrated that, selecting $n_{c2}/n_{c1} = \sqrt{3}$, the sub–harmonic of order $\nu = 1$ disappears [34, 35].

However, the winding arrangement has not effect on all harmonics. There are some harmonics which can not be reduced changing the winding arrangement and their winding factor remains the same of the winding factor of the main harmonic (i.e., whose order is $\nu = p$). They are the so-called slot–harmonics. Their order is expressed as:

$$\nu_{sh} = k \cdot Q \pm p \tag{2.19}$$

where k is an integral number. In the 12–slot 10–pole machine, their order is 7 and 17 (k = 1), 19 and 29 (k = 2), and so on.

Then, as the second step of the optimization procedure, an accurate analysis of the rotor geometry is carried out. The optimal flux–barrier angles have to be selected, since they mainly affects the torque ripple [17, 21, 23]. In particular, the rotor geometry has to be optimized to reduce the torque ripple associated to the slot harmonics.

Since the torque harmonics vary in amplitude and in phase according to the position of the flux–barrier angles ϑ_{b1} and ϑ_{b2}, shown in Fig. 2.29, it is possible to select couples of flux–barrier angles (θ_{b1} – θ_{b2}) exhibiting torque harmonics with the same amplitude but opposite phase. The rotor is designed according to these

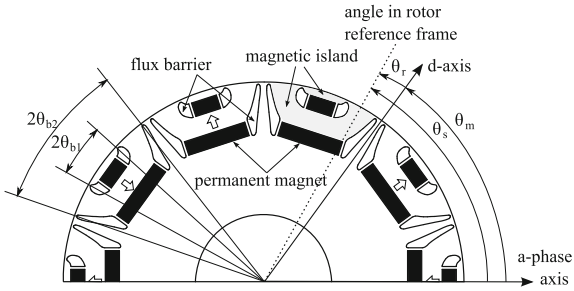

Fig. 2.29 Rotor geometry, flux–barrier angles and reference angles

flux–barrier angles. It results asymmetric (of "machaon" type, as described above) since the two rotor poles forming each pole pairs are different.

To evaluate the performance of those optimal machines, the average torque and the torque ripple have been computed along the four trajectories: the MTPA trajectory, the minimum torque ripple (MTR) trajectory, the constant $\alpha_i^e = 35°$ trajectory (which well approximates the MTPA one), and the constant $\alpha_i^e = 45°$ trajectory (which well approximates the MTR one).

Figure 2.30 shows the torque ripple along different trajectories. It could be noted that the torque ripple results to be always lower than 5 %, regardless to the adopted trajectory. The lowest values of torque ripple achieved along the MTR trajectory are almost equal to those achieved along the $\alpha_i^e = 45°$ trajectory. By comparing the torque ripple along the MTPA and the MTR trajectories, a low difference could be noted.

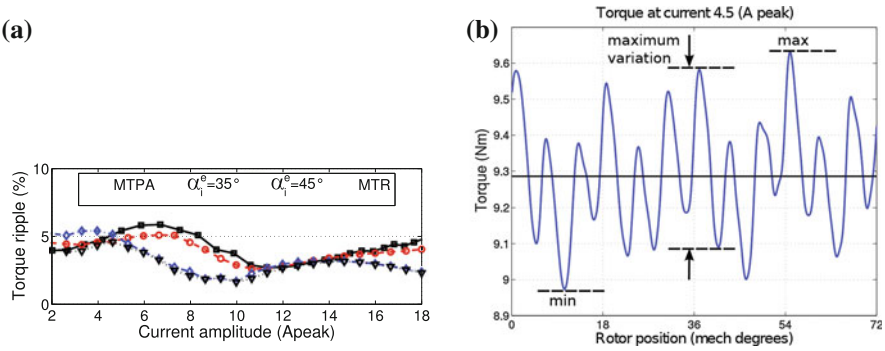

Fig. 2.30 Ripple of a fractional–slot winding IPM machine, after the two–step optimization. The torque ripple is computed along different control trajectories

2.11 Conclusions

This chapter dealt with the synchronous REL motor and the PM assisted REL motor. The basic operating principles were briefly summarized, highlighting advantages and drawbacks of these machines. The impact of the PM on the machine performance was pointed out. Techniques to limit the torque ripple are proposed, for both distributed winding and fractional–slot winding machines. Vector control techniques are described including maximum torque per Amps control and flux–weakening control. Then, the key concepts of sensorless rotor position control are described.

Acknowledgments The author is very grateful to Prof. Silverio Bolognani for his helpful suggestions, to Eng. Mosé Castiello for his help during motor tests, to Dr. Luigi Alberti, Dr. Massimo Barcaro, and Dr. Emanuele Fornasiero for their help in simulations and tests. The author thanks Dr. Michele Dai Pré (Calpeda SpA), Mr. Massimo Trova (Magnetic SpA), and Mr. Alberto Pace (SME group) for their help in assembling the motor prototypes.

References

1. Fratta, A., Vagati, A., Villata, F.: Permanent magnet assisted synchronous reluctance drive for constant-power application: Drive power limit. In: Proceedings of the Intelligent Motion European Conference, PCIM, pp. 196–203. April Nurnberg, Germany (1992)
2. Kim, W.H., Kim, K.S., Kim, S.J., Kang, D.W., Go, S.C., Chun, Y.D., Lee, J.: Optimal PM design of PMA-SynRM for wide constant-power operation and torque ripple reduction. IEEE Trans. Magn. **45**(10), 4660–4663 (2009)
3. Liwschitz-Garik, M., Whipple, C.C.: Electric Machinery, vol. II, A–C Machines. D. Van Nostrand Company Inc., New York (1960)
4. Bianchi, N.: Electrical Machine Analysis using Finite Elements. Power Electronics and Applications Series. CRC Press, Taylor & Francis Group, Boca Raton, FL, USA (2005)
5. Bianchi, N.: Analysis of the IPM motor—Part I, analytical approach. In: Bianchi, N., Jahns T.M. (eds.) Design, Analysis, and Control of Interior PM Synchronous Machines. IEEE IAS Tutorial Course Notes, IAS Annual Meeting, CLEUP, Seattle, October 3, 2005, Chapter 3, pp. 3.1–3.33. info@cleup.it
6. Bianchi, N., Dai Pré, M., Bolognani, S.: Design of a fault-tolerant IPM motor for electric power steering. In: Proceedings of the IEEE Power Electronics Specialist Conference, PESC'05, 12–16 June 2005
7. Welchko, B.A., Jahns, T.M., Soong, W.L., Nagashima, J.M.: IPM synchronous machine drive response to symmetrical and asymmetrical short circuit faults. IEEE Trans. Energy Convers. **EC-18** (2003)
8. Jahns, T.: Flux-weakening regime operation of an interior permanent-magnet synchronous motor drive. IEEE Trans. Ind. Appl. **IA-23**(4), 681–689 (1987)
9. Morimoto, S., Takeda, Y., Hirasa, T., Taniguchi, K.: Expansion of operating limits for permanent magnet motor by current vector control considering inverter capacity. IEEE Trans. Ind. Appl. **26**(5), 866–871 (1990)
10. Soong, W., Miller, T.: Field-weakening performance of brushless synchronous AC motor drives. IEE Proc. Electr. Power Appl. **141**(6), 331–340 (1994)
11. Jansen, P.L., Lorenz, R.D.: Transducerless position and velocity estimation in induction and salient AC machines. IEEE Trans. Ind. Appl. **31**(2), 240–247 (1995)

12. Jahns, T.: Flux–weakening regime operation of an interior permanent magnet synchronous motor drive. IEEE Trans. Ind. Appl. **IA–23**(3), 681–689 (1987)
13. Wang, L., Lorenz, R.D.: Rotor position estimation for permanent magnet synchronous motor using saliency-tracking self-sensing method. In: Conference Record of the 2000 IEEE Industry Applications, vol. 1, pp. 445–450 (2000)
14. Bianchi, N., Bolognani, S., Jang, J.-H., Sul, S.-K.: Comparison of PM motor structures and sensorless control techniques for zero-speed rotor position detection. IEEE Trans.Power Electron. **22**(6), 2466–2475 (2007)
15. Guglielmi, P., Pastorelli, M., Vagati, A.: Cross-saturation effects in ipm motors and related impact on sensorless control. IEEE Trans. Ind. Appl. **42**(6), 1516–1522 (2006)
16. Fratta, A., Troglia, G.P., Vagati, A., Villata, F.: Evaluation of torque ripple in high performance synchronous reluctance machines. In: Records of IEEE Industry Application Society Annual Meeting, vol. I, pp.163–170. October Toronto, Canada, 1993
17. Vagati, A., Pastorelli, M., Franceschini, G., Petrache, S.C.: Design of low-torque-ripple synchronous reluctance motors. IEEE Trans. Ind. Appl. **IA-34**(4), 758–765 (1998)
18. Jahns, T.M., Soong, W.L.: Pulsating torque minimization techniques for permanent magnet AC motor drives—A review. IEEE Trans. Ind. Electr. **IE-43**(2), 321–330 (1996)
19. Han, S.H., Jahns, T.M., Soong, W.L., Guven, M.K., Illindala, M.S.: Torque ripple reduction in interior permanent magnet synchronous machines using stators with odd number of slots per pole pair. IEEE Trans. Energy Convers. **25**(1), 118–127 (2010)
20. Bianchi, N., Bolognani, S.: Reducing torque ripple in PM synchronous motors by pole shifting. In: Proceedings of the International Conference on Electrical Machines, ICEM, Aug. Helsinki (2000)
21. Sanada, M., Hiramoto, K., Morimoto, S., Takeda, Y.: Torque ripple improvement for synchronous reluctance motor using an asymmetric flux barrier arrangement. IEEE Trans. Ind. Appl. **40**(4), 1076–1082 (2004)
22. Li, T., Slemon, G.: Reduction of cogging torque in permanent magnet motors. IEEE Trans. Mag. **24**(6), 2901–2903 (1988)
23. Bianchi, N., Bolognani, S., Bon, D., Dai Pré, M.: Rotor flux-barrier design for torque ripple reduction in synchronous reluctance and PM-assisted synchronous reluctance motors. IEEE Trans. Ind. Appl. **45**(3), 921–928 (2009)
24. Barcaro, M., Bianchi, N.: Interior PM machines using ferrite to substitute RareEarth surface PM machines. In: Conference Record of the International Conference on Electrical Machines, ICEM, Marsille (F), pp. 1–7, June 2012
25. EL-Refaie, A.: Fractional-slot concentrated-windings synchronous permanent magnet machines: Opportunities and challenges. IEEE Trans. Industr. Electron. **57**(1), 107–121 (2010)
26. Cros, J., Viarouge, P.: Synthesis of high performance PM motors with concentrated windings. IEEE Trans. Energy Convers. **17**(2), 248–253 (2002)
27. Bianchi, N., Dai Prè, M., Grezzani, G., Bolognani, S.: Design considerations on fractional-slot fault-tolerant synchronous motors. IEEE Trans. Ind. Appl. **42**(4), 997–1006 (2006)
28. Barcaro, M., Bianchi, N., Magnussen, F.: Analysis and tests of a dual three-phase 12-slot 10-pole permanent-magnet motor. IEEE Trans. Ind. Appl. **46**(6), 2355–2362 (2010)
29. Park, J.M., Kim, S.I., Hong, J.P., Lee, J.H.: Rotor design on torque ripple reduction for a synchronous reluctance motor with concentrated winding using response surface methodology. IEEE Trans. Magn. **42**(10), 3479–3481 (2006)
30. Ionel, D.: Interior permanent magnet motor including rotor with unequal poles. U.S. Patent, 8,102,091, Jan. 24, 2102
31. Magnussen, F., Lendenmann, H.: Parasitic Effects in PM Machines With Concentrated Windings. IEEE Trans. Ind. Appl. **43**(5), 1223–1232 (2007)
32. Barcaro, M., Bianchi, N.: Torque ripple reduction in fractional-slot interior pm machines optimizing the flux-barrier geometries. In: International Conference on Electrical Machines, ICEM, Sept. 2012 (2012)

33. Alberti, L., Barcaro, M., Bianchi, N.: Design of a low torque ripple fractional-slot interior permanent magnet motor. In: Conference Record of the 2012 IEEE Energy Conversion Conference and Exposition, ECCE, Raleigh NC, USA, vol. 1, pp. 1–8 (2012)
34. Cistelecan, M.V., Ferreira, F.J.T.E., Popescu, M.: Three phase tooth-concentrated multiple-layer fractional windings with low space harmonic content. In: 2010 IEEE Energy Conversion Congress and Exposition, ECCE, pp. 1399–1405 (2010)
35. Alberti, L., Bianchi, N.: Theory and design of fractional-slot multilayer windings. In: Energy Conversion Congress and Exposition, ECCE, 2011 IEEE, Sept. 2011, pp. 3112–3119

http://www.springer.com/978-3-319-32200-1

The Rediscovery of Synchronous Reluctance and Ferrite Permanent Magnet Motors
Tutorial Course Notes
Pellegrino, G.; Jahns, Th.M.; Bianchi, N.; Soong, W.; Cupertino, F.
2016, VIII, 136 p. 129 illus., 47 illus. in color., Softcover
ISBN: 978-3-319-32200-1